



# Synchrotron X-ray imaging and ultrafast tomography in situ study of the fragmentation and growth dynamics of dendritic microstructures in solidification under ultrasound

Zhiguo Zhang<sup>a,b</sup>, Chuangnan Wang<sup>b</sup>, Billy Koe<sup>b,c</sup>, Christian M. Schlepütz<sup>d</sup>, Sarah Irvine<sup>c</sup>, Jiawei Mi<sup>b,e,\*</sup>

<sup>a</sup> Institute of Advanced Wear & Corrosion Resistant and Functional Materials, Jinan University, Guangzhou, 510632, China

<sup>b</sup> Department of Engineering, University of Hull, East Yorkshire HU6 7RX, UK

<sup>c</sup> Diamond Light Source, Harwell Science and Innovation Campus, Didcot, Oxfordshire OX11 0DE, UK

<sup>d</sup> Swiss Light Source, Paul Scherrer Institute, 5232 Villigen, Switzerland

<sup>e</sup> School of Materials Science and Engineering, Shanghai Jiao Tong University, Shanghai, 200240, China

## ARTICLE INFO

### Article history:

Received 26 July 2020

Revised 28 February 2021

Accepted 6 March 2021

Available online 14 March 2021

### Keywords:

Synchrotron X-ray imaging

Ultrafast synchrotron X-ray tomography

Ultrasound melt processing

Dendrite fragmentation

Solidification

Al alloys

## ABSTRACT

High speed synchrotron X-ray imaging and ultrafast tomography were used to study *in situ* and in real time the fragmentation and growth dynamics of dendritic microstructures of an Al-15%Cu alloy in solidification under ultrasound. An ultrasound of 30 kHz with vibration amplitude of 29  $\mu\text{m}$  was applied into the alloy melt and produced a strong swirling acoustic flow of  $\sim 0.3$  m/s. Efficient dendrite fragmentation occurred due to the acoustic flow and the dominant mechanism is the thermal perturbation remelting plus mechanical fracture and separation effect. Acoustic flow fatigue impact and phase collision effects were found to play a minor role in causing dendrite fragmentation. Just 10 s of ultrasound application at the early stage of solidification produced  $\sim 100\%$  more dendrite fragments compared to the case without ultrasound, resulting in 20–25% reduction in the average grain size in the solidified samples. Furthermore, the dendrite morphology and tip growth velocity were mainly affected by the initial dendrite fragment number density and their distribution. The systematic and real-time datasets obtained in near operando conditions provided valuable 4D information for validation of numerical models and assistance in developing optimisation strategy for ultrasound melt processing in industry.

© 2021 The Authors. Published by Elsevier Ltd on behalf of Acta Materialia Inc.

This is an open access article under the CC BY license (<http://creativecommons.org/licenses/by/4.0/>)

## 1. Introduction

Ultrasound melt processing (USMP) is a physical field-based method for degassing in liquid metals and refining solidification microstructures [1,2]. Compared to the conventional methods routinely used in metal industry, for example, degassing of Al alloy melts using inert gases (or chlorine gas or chloride containing salt fluxing), and grain refinement using external grain refiners, the unique advantages of USMP are: (1) it is generic and applicable to virtually all alloy systems regardless of the alloy chemistry (on the condition that sufficient ultrasound intensity can be produced in the alloy melt); (2) it is environmentally friendly and operationally efficient without the need of adding external chemicals into the processed melt [2,3].

Since the 1930s, researchers have used conventional solidification experiments followed by post-solidification microstructural characterisation methods to study the mechanisms of microstructure refinement in different alloy systems due to the application of ultrasound [3–9]. Most recently, ultrasound has also been demonstrated to be very effective in refining the microstructure and improving chemistry homogeneity in the metal additive manufacturing processes [10]. So far, two important mechanisms have been widely accepted, namely the effect of ultrasonic cavitation and that of ultrasonic streaming flow during USMP [9,11]. Ultrasonic cavitation is the process of nucleating cavities and bubbles in liquids, and the subsequent bubble oscillation, growth and implosion under an alternating acoustic pressure. These are highly dynamic and non-linear phenomena when occurring in solidifying metals, resulting in cavitation-enhanced grain nucleation and cavitation-induced structure fragmentation. Both increase the number of the initial dendrite fragments inside the melt, leading to refined grain structures [4,9]. However, until the recent reports on real-time

\* Corresponding author.

E-mail address: [J.Mi@hull.ac.uk](mailto:J.Mi@hull.ac.uk) (J. Mi).

studies of ultrasonic bubble dynamics in liquid metals [9,11–13], there are very limited real-time imaging data and visual evidence obtained *in situ* from liquid metals to support the above hypotheses of cavitation-enhanced nucleation and cavitation-induced fragmentation. The detailed interactions between growing phases and acoustic streaming flow, and the quantitative effects of acoustic flow on dendrite fragmentation and dendrite growth in operando conditions, especially in three-dimensional (3D) space still remain unclear.

There has been a worldwide, renewed interest in the materials manufacturing and metallurgy sector to further develop and scale up ultrasound-based liquid metal processing technologies [3]. This motivates the uses of *in situ* and real time characterization techniques to study the dynamics in liquid melt under USMP. Concurrently, since the late 1990s, a number of the 3<sup>rd</sup> generation synchrotron X-ray facilities around the world have developed high-speed radiography and tomography capabilities that allow materials scientists and engineers to study in real time and *in situ* the dynamics of microstructure evolution in metal solidification processes. Hence, numerous research groups have recently taken advantage of these new capabilities and used synchrotron X-ray radiography (2D imaging) to study ultrasonic bubble dynamics in liquid metals [5,14–16]. For example, Huang et al. [14], Xu et al. [15] and Mirihanage et al. [5] studied the size distribution, average radius, growth rate and number density of ultrasonic bubbles in Al-Cu alloys. Tzanakis et al. reported the instantaneous re-filling of a micro-capillary channel by liquid metal due to the ultrasonic capillary effects [16]. However, the image acquisition speeds used in the above studies were in the range of 1 to 63 frames per second (fps), unable to reveal the true dynamic behaviour of ultrasonic bubbles and acoustic streaming flow in liquid metals.

Recently, we used ultrafast synchrotron X-ray imaging (up to 271,554 fps) to capture shockwaves and enhanced acoustic liquid metal flows in Sn-13%Bi and Bi-8%Zn alloys [9,11–13]. This allowed us to observe *in situ* the fragmentation of intermetallic phases by oscillating bubbles and the break-up of solid-liquid interfaces by an acoustic streaming flow [9,11–13, 17]. Such unambiguous real-time evidence elucidated that the acoustic streaming flow (an enhanced fluid flow produced and driven by acoustic pressure) is very effective in disrupting the growth of intermetallic phases and the growing liquid-solid interface in the semi-solid state.

However, those phenomena were observed in a thin channel of approximately 0.3 mm thickness [11–17]. Such a geometrical constraint in the thickness direction may restrict the free growth of solidifying phases and the development of the acoustic flow field. Hence, the velocity field of the acoustic streaming flow observed may not be representative to that occurred in a bulk sample under USMP.

In addition, 2D radiography is not able to capture the true 3D morphological development or evolution of solidification phases often found in a bulk sample with a size range of a few to a few tens of millimetres. Recently, measurements of the 4D microstructure evolution (3D tomography plus time) in Al alloys [18–20] and Mg alloys [21–23] have been carried out, providing much more quantitative insights into the formation and evolution of primary dendrites, intermetallic compounds and solidification defects. However, they were all conducted in relative equilibrium and/or iso-thermal solidification conditions. Few of these studies included any use of external fields in their tomography experiments. The reasons are: it is a technical and experimental challenge to perform precise experiments of growing metal dendrites and applying external fields including ultrasound simultaneously. Especially difficult in maintaining them in the same field of view (FOV) in a highly dynamic solidification process for continuous radiography and/or tomography acquisition. In addition, the sheer amount of image data acquired in a short time frame (many GB in a sec-

ond) must be transferred from the camera to storage on external disks or servers. The fast-access on-board memory capacity of most high-speed cameras (often in 8–128 GB range) is usually not sufficient to record and store continuously all X-ray projections (especially the large tomography datasets, normally in a few TB range) during the whole solidification process. However, typical transfer rates from the camera memory board to external storage are much slower than the incoming imaging data rate, thus quickly saturating the storage capacity of the camera imaging system. As a result of these obstacles, the interaction between ultrasonic bubbles/streaming flow and growing dendrites were so far only studied in 2D in organic transparent alloys by optical high-speed imaging but not tomography [24,25]. Until now, the dynamic interactions between ultrasonic bubbles/acoustic streaming flow with solidifying dendritic grains, in particular 3D information on the dendritic structures, has not been reported.

In this paper, we report on the design and use of a dedicated sample holder arrangement with sufficient internal volume space for liquid metal flow to develop and dendrites to grow. The aim is to achieve realistic and near *operando* solidification conditions under USMP in a geometry compatible with continuous high-speed radiography and tomography scans during the whole solidification process. Such an arrangement allowed us to switch seamlessly between 2D imaging and 3D tomography to study in real time the dynamic interactions between ultrasound streaming flow and 3D growing dendritic grains in an Al-15wt%Cu alloy under USMP. The synchrotron X-ray real-time imaging and tomography data were collected at the Tomographic Microscopy and Coherent radiology experiment (TOMCAT) beamline of the Swiss Light Source. Analyses of those datasets provide unambiguous evidence for us to understand the mechanism of how the swirling flow is created in the region under the sonotrode, and how the interaction between the acoustic flow and growing dendrites leads to the fragmentation and refinement of the dendritic structures. This information is essential for validating numerical models that simulate dendritic grain evolution under external fields and for developing USMP optimisation strategy in industry.

## 2. Experimental methods

### 2.1. 2.1 Alloys and experimental setup

A hypoeutectic Al-15%Cu (weight percent) alloy made from high-purity Al (99.99 pct) and Cu (99.99 pct) was used as the experimental alloy because of sufficient X-ray absorption contrast between the Cu-enriched liquid and  $\alpha$ -Al primary dendritic phases [26].

Fig. 1 shows a schematic of the experimental setup for the *in-situ* synchrotron imaging and tomography experiments at the

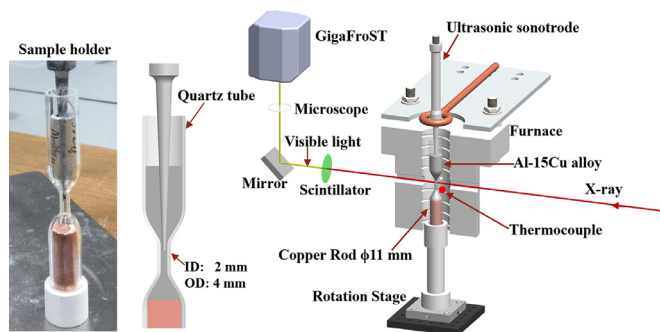
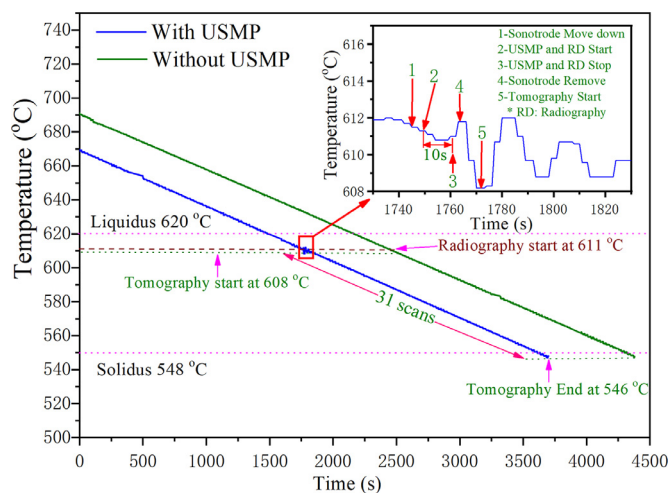


Fig. 1. A schematic of the experimental setup and the special quartz sample holder arrangement for *in-situ* synchrotron imaging and tomography of the solidification of an Al-15wt%Cu alloy under ultrasound.



**Fig. 2.** The temperature profiles recorded during cooling of the Al-15%Cu alloys. The insert shows the enlarged temperature profile when the sonotrode tip was moved into the melt, and then ultrasound was started. The ultrasound was applied for 10 s, and then the sonotrode was lifted out of the melt. Tomography scan started at 608 °C until the melt cooled down to 546 °C. The cooling rate was 2 °C/min. (The measured temperature profile, i.e. the green line, for the case without USMP is offset vertically by 20 °C for better visualisation and easy comparison)

TOMCAT beamline [27]. The sample holder was made from a quartz tube with variable cross-sections, as shown in Fig. 1. In the middle, there was a small diameter tube section (2 mm ID, 4 mm OD and 10 mm tall) for X-ray to pass through in radiography and tomography acquisition. A copper rod (11 mm diameter and 30 mm tall) was positioned at the bottom of the quartz tube, acting as a heat sink. A K-type thermocouple (0.25 mm diameter wire) was placed very close to the middle point of the quartz tube to monitor and record temperature. It was not feasible to insert the thermocouple directly into the alloy melt to measure its temperature *in situ* because (1) the rotation during tomography scans could entangle the thermocouple wire, (2) The presence of thermocouple in the melt would interfere the nucleation and growth of Al dendrites. To ensure and maintain a consistent and repeatable heating and cooling conditions for all experiments, temperature calibration experiments were made for the Al-15%Cu alloy and repeated four times as detailed in Section 2.2 and Fig. 2. Real time radiography observation allowed us to see, at what temperature recorded from this thermocouple, the dendritic grains appeared in the field of view (FOV) and then image recording was triggered. Such experimental protocol was used for all samples during the radiography and tomography acquisition.

A Hielscher UP100H ultrasound processor and specially designed and custom-made pure niobium sonotrodes with a 1 mm diameter tip were used to generate ultrasonic waves into the Al melt. The design, making and testing of the bespoke Nb sonotrodes are described in Section 1 of the Supplementary Materials. The ultrasound processor was placed on a  $\mu\text{m}$ -step precision linear stage in order to move accurately the sonotrode tip vertically into or out of the Al melt. The applied ultrasonic wave frequency was 30 kHz. The sonotrode tip null-to-peak amplitude in the Al-15%Cu melt was measured from the X-ray radiography images, and it was 29  $\mu\text{m}$ . Under this condition, the acoustic power density in the Al-15%Cu melt was estimated as  $\sim 27.9 \text{ W/cm}^2$  (see Section 2 of Supplementary Materials). This value is lower than the threshold required for developing cavitation in Al melt ( $\sim 30 \text{ W cm}^{-2}$ ) [2]. In addition, the X-ray radiography showed that with such ultrasound energy input, only a strong swirling streaming flow was produced. No visible cavitation bubble zone was developed under the

sonotrode tip. Therefore, the *in situ* observed phenomena were the results of acoustic flow.

## 2.2. Experimental parameters

Table 1 lists the detailed experimental parameters used for 2D imaging and 3D tomography acquisition at TOMCAT. The full white beam from the 2.9 T superbend was used for imaging. It was filtered by a 400  $\mu\text{m}$  thick Al foil plus 5 mm of glassy carbon to suppress the low energy content. The sample was located approximately 25 m away from the source and 180 mm before the scintillator, which is made of 100  $\mu\text{m}$  thick LuAG:Ce. The visual light emitted by the scintillator was coupled onto the imaging chip of the GigaFRoST camera system with a pixel size of 11.0  $\mu\text{m}$  via an optical light microscope with  $6.8 \times$  magnification, resulting in an effective pixel size of 1.62  $\mu\text{m}$ . The FOV of the camera was adjusted to a region of interest of  $1392 \times 1700$  pixels to cover the full width of the small diameter middle tube region for imaging, while reducing as much as possible the amount of unnecessary data to be acquired.

The GigaFRoST high-speed camera and readout system available at TOMCAT is capable of streaming the acquired imaging data directly onto the data back-end server with a high data throughput of nearly 8 GB/s [28]. This eliminates the bottleneck in the data acquisition and transfer described previously, which is often found in cameras with limited on-board memory, while also allowing for a live preview of the projection images. Using these advanced capabilities, we scanned all samples using a predefined measurement protocol in well-defined experimental conditions over the entire solidification process, making it possible to quantify the relevant microstructural evolution in the whole cooling process.

Prior to the imaging experiments, the Al-15%Cu alloy was re-melted four times with USMP treatments to ensure a homogeneous composition. The sample was then heated to 720°C and held for 10 min to ensure a homogenous melt temperature (the liquidus of the hypoeutectic Al-15%Cu is 620°C [29]). The sonotrode tip was then moved down into the FOV and located at the middle region of the small diameter tube. The liquid melt was subsequently cooled with a cooling rate of  $\sim 2^\circ\text{C}/\text{min}$ . Fig. 2 shows the recorded temperature profiles and when radiography and tomography scans were taken. The appearance of dendrites and their growth dynamics in the FOV were observed and recorded by radiography. When the melt temperature reached 611°C, 2D-radiographic imaging started at 1000 fps and USMP treatment was activated. The duration of USMP was set to 10 s. After that, the sonotrode tip was lifted out of the melt, and the sample stage was rotated with a speed of 90 degree/s to acquire tomography scans (started at 608°C) for the subsequent entire solidification process. For each tomography scan, 2000 projections were acquired over 180 degree of sample rotation; each at an exposure time of 1.0 ms, resulting in a total scanning time of 2 s per tomography. Scans were acquired once per minute while maintaining the cooling rate of  $2^\circ\text{C}/\text{minute}$ . At this cooling rate, the time resolution of such a scanning protocol was sufficient to capture the complete dynamic evolution of the dendrites. Overall, 31 tomograms were collected during the solidification process before the alloy solidified completely, i.e. the whole solidification process of the Al-15%Cu alloy was recorded within 31 minutes. The corresponding temperature at the end of the scan series was 546°C, just below the eutectic temperature of 548°C [29]. The sample was then re-heated back to 720°C. Such temperature control protocol was repeated 4 times to ensure that at each heating and cooling cycle, a consistent and repeatable cooling rate was achieved (as evidenced in Fig. 2) before data acquisition started. A baseline reference sample with identical cooling parameters without USMP was also measured. In the enlarged insert of Fig. 2, the small variation of temperature in the case of USMP was due to

**Table 1**  
Parameters for the radiography and tomography acquisition at TOMCAT

X-ray beam	White beam (filtered by a 400 $\mu$ m Al foil + 5 mm carbon)
Scintillator	LuAG:Ce 100 $\mu$ m
Camera	GigaFRoST
Pixel size	11.0 $\mu$ m
Optical microscope	Optique Peter white beam microscope
Effective magnification	6.8 $\times$
Effective pixel size	1.62 $\mu$ m
Field of View	1392 $\times$ 1700 pixels
Exposure time	1.0 ms
Sample-to-scintillator distance	180 mm
Image acquisition rate (radiography & tomography)	1000 fps
No. of projections for 3D tomography	2000

the application of ultrasound and movement of the sonotrode. Although at the time points 4 and 5 (the insert of Fig. 2), it showed that there was 3–4  $^{\circ}$ C variation at the thermocouple tip region due to the movement of the sonotrode. Actual variation of the real temperature (the measurement error) of the melt inside the quartz tube was in a range of approximately  $\pm 1$   $^{\circ}$ C as confirmed many times in the temperature calibration runs and other similar experiments using the similar set up at TOMCAT in the past.

### 2.3. Image processing

The 2D radiography images were processed by a custom macro program written in the open-source image processing software, Fiji [30], which included flat-field correction [31], an FFT filter and a bandpass filter. 3D tomography reconstruction was performed using the Savu processing pipeline software developed by Diamond Light Source [32]. The ASTRA Recon GPU implementation based on a filtered-back projection algorithm was also applied [33]. In order to improve the image quality for segmentation, the reconstructed 3D datasets were further filtered by a contrast-limited adaptive histogram equalization (CLAHE) filter in the Fiji software [34]. 3D tomographic image segmentation and rendering were conducted using Avizo 9.4 software (FEI VSG, France). A watershed method was applied to segment the primary  $\alpha$ -Al phase, the liquid phase and void spaces in the sample. For quantitative statistical analysis of the 3D features in the segmented datasets, a high-level combination module with watershed, distance transform and numerical reconstruction algorithms in the Avizo (<https://www.fei.com/software/amira-avizo/>) was also used to separate the dendrites in 3D datasets and 2D projections.

## 3. Results

### 3.1. Real-time visualisation of the flow dynamics under ultrasound

Fig. 3 shows the typical radiography images with and without USMP at the selected time steps. The sonotrode tip was seen at the top-right delineated by the dotted lines in the figure. The time for the first image in the image sequences was referenced as  $t = 0$  s; and note that such zero-time reference is different to that showed in the temperature profile (Fig. 2). The corresponding image sequences are showed in the supplementary Video #1, illustrating more clearly the vivid and dynamic information.

Before USMP was applied, in the FOV, a few cellular-type solid grain clusters (marked by the dotted yellow lines in Fig. 3a) appeared near the quartz sample holder wall. They formed due to a small thermal gradient between the quartz wall and the liquid alloy. A long primary  $\alpha$ -Al dendrite arm was also observed to appear at the bottom of the FOV. This dendrite was one primary dendrite arm that grew from below the FOV due to the thermal gradient generated by the copper rod at the bottom of the sample holder.

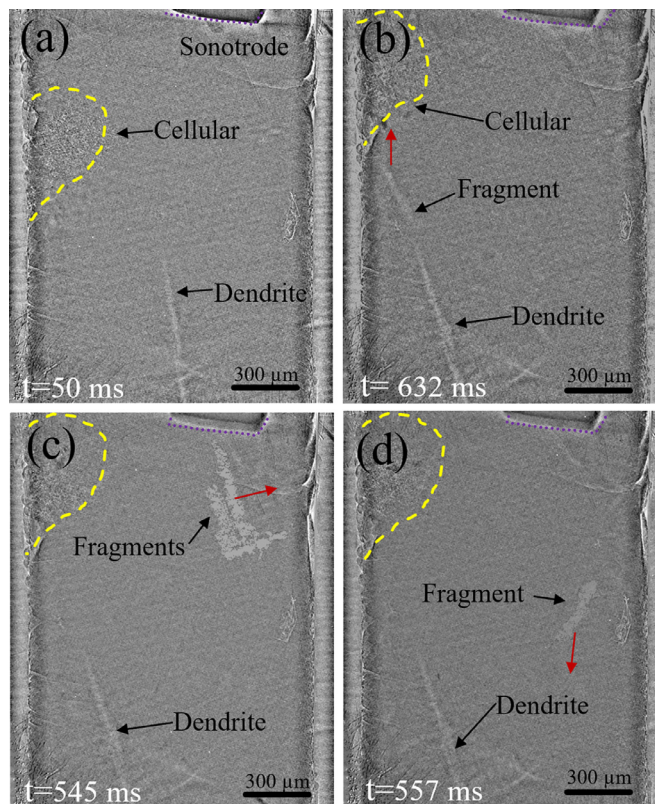


**Fig. 3.** Selected radiographic images of the Al-15%Cu alloy in solidification without and with USMP. (a) the steady-state melt condition and an anchored long  $\alpha$ -Al dendrite before USMP; (b) showing the movement of the long dendrite, other fragments and a cellular grain cluster after USMP was triggered; (c) and (d) illustrating the collision between the moving dendrites and the growing dendrites near the tube wall (see video #1 for the vivid dynamic information).

The alloy melt without USMP showed a steady-state characteristic with virtually no apparent movement of the grains or dendrites (see Video #1).

In contrast, the radiography images with USMP revealed a series of dynamic events (Fig. 3b-d and Video #1). Immediately after the ultrasound was triggered, a significantly enhanced acoustic flow occurred as clearly illustrated in Video #1. The acoustic flow swirled in a clockwise direction below the sonotrode tip. Its average velocity was approximately 0.3 m/s, measured from the movement of several oxides and free dendrite fragments in the melt flow over several consecutive frames in the 2D image sequences. The results obtained for the acoustic flow velocity and flow features agreed with our previous observation in Al-35%Cu alloys [17] and the computational fluid dynamics modelling results in liquid aluminium [35]. This specially designed sample holder al-

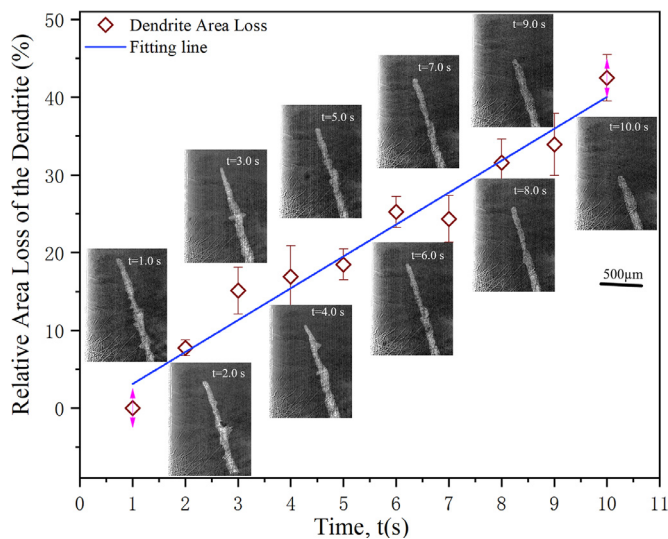


**Fig. 4.** Fragmentation of the long primary dendrite arm during the USMP, and the relative area loss of this dendrite arm over the applied 10 s USMP period (see video #2 for the dynamic information).

lowed the swirling acoustic flow driven by ultrasound to be visualised in the whole liquid metal flow field. It is different from what we have found in a thin sample holder [9,17], where only limited local flow features were observed. The long primary dendrite arm at the bottom of the FOV was observed to move from the middle to the left, driven by the swirling acoustic flow, as marked in Fig. 3b. Meanwhile, the cellular grain clusters located at the top left expanded, moved and partially disintegrated under the acoustic flow, showing clearly part of the grain cluster was decomposed into small crystal fragments by the swirling acoustic flow (towards the end of Video #1). Some grey-white dendrite fragments were found to follow planetary movement inside the swirling flow in the ultrasound field. These dendrite fragments originated from the bottom of the FOV and the tube wall under acoustic flow stirring, indicating that the dendrite fragments were mainly due to the detachment from the growing primary  $\alpha$ -Al dendrite arms rather than any naturally grown dendrites in the melt inside the FOV. A typical dendrite fragment from the bottom of the FOV was illustrated in Fig. 3b and its moving direction was marked by the red arrow. Fig. 3c and d show the dynamic movement and collision between the moving dendrite fragments and the growing dendrites near the tube wall, illustrating clearly the multiplication effects of dendrite fragments. Video #1 shows more clearly the dynamic movement and impact among those dendrites.

Fig. 4 and video #2 (image frames at 100 ms intervals were selected to show the whole 10 s USMP period) show the morphology evolution of the long primary dendrite arm (the one showed in Fig. 3a is enlarged here for easy visualization) under the 10 s USMP. Comparing with video #2, the image contrast in Fig. 4 was further enhanced. As described above, this dendrite arm moved from the centre of the FOV to the left after the initial activation of ultrasound and then stayed at that position for the duration of USMP.

The most interesting phenomenon is that, as the dendrite continuously interacted with the oncoming acoustic flow, its length was gradually shortened from 1.2 mm to 0.6 mm and part of its tip disappeared. The relative area loss ratio of this dendrite in 2D radiography over the applied 10 s USMP period is shown in Fig. 4, where the plane dendrite area at  $t=1.0$  s was referenced as the initial dendrite area. As seen in the figure, the area loss of the dendrite exhibited a nearly linear relationship with USMP treatment time. A total of 42.5% area loss for this dendrite was recorded in

the 10 s USMP period. The loss of the dendrite was due to the effect of thermal remelting coupled with mechanical fracture under the acoustic flow [17,26], which is the most important mechanism for the dendrite fragmentation.

### 3.2. Dendrite fragments and their spatial distribution at the early stage of solidification

Immediately after USMP, continuous ultrafast tomography was taken to capture the 3D spatial distribution of the dendrite fragments caused by USMP. Fig. 5 shows the initial three tomograms for the cases without (Fig. 5a-c) and those with (Fig. 5d-f) USMP. For all cases, the volume fraction of Al dendrites with USMP in the FOV was much higher than the corresponding case without USMP, indicating that USMP led to a significant increase in the numbers of dendrite fragments in the melt. For example, the volume fraction of Al dendrites in the 1<sup>st</sup> tomogram ( $T=608$  °C) with USMP was 12.8% while that for the case without USMP was 5.5%. In the 2<sup>nd</sup> and the 3<sup>rd</sup> tomogram ( $T=606$  °C,  $T=604$  °C), the volume fraction of Al dendrites with USMP became 10.8% and 15.2% while the corresponding data without USMP were 2.0% and 4%. It was also noticed that, from the 1<sup>st</sup> tomogram to the 2<sup>nd</sup> one (for both cases with and without USMP), there were some apparent changes in the numbers of dendrites and their spatial positions. This was caused by the sudden start-up of sample rotation in the 1<sup>st</sup> tomography scan. The sudden acceleration of the quartz tube holder from a static condition ( $0^\circ/\text{s}$ ) to an angular speed of  $90^\circ/\text{s}$  resulted in an instantaneous melt movement in the circumferential direction. Hence, the dendrites originally attached onto (or near) the quartz tube inner wall (i.e. the peripheral region of the tomography renderings showed in Fig. 5a and d) were detached and/or moved away. This was evidenced by the decreased number of the dendrites located near the peripheral region of the tomography renderings in Fig. 5b and e respectively. Some of the detached dendrite fragments moved upwards and out of the FOV. However, after the 1<sup>st</sup> tomogram, the melt regained a relatively steady state in a constant rotating and continuous cooling condition. The dendrites and their spatial positions became relatively stable from the 2<sup>nd</sup> tomogram onwards. Hence the counted volume number of the dendrite fragments from the 2<sup>nd</sup> scan onwards was consistent and the trend was representative from statistics point of view. We therefore used the data from the 2<sup>nd</sup> tomogram as the baseline data point for the subsequent statistical analysis.

For this particular alloy, the distribution of the dendrite fragments at the initial solidification stage was inhomogeneous in the FOV. As shown in Fig. 5b-c and e-f, the dendrite fragments tended to gather at the top and the bottom regions of the FOV, regardless of the presence of USMP. For example, the dendrite volume fraction reached 25% in the top 1/3 section of the FOV in the 2<sup>nd</sup> tomogram with USMP (Fig. 5e), greater than that in the middle 1/3 section (16%) and the bottom 1/3 section (18%). The accumulation of dendrite fragments at the top was due to the buoyancy of the broken dendrite fragments as they had a lower density than the surrounding melt. On the other hand, more dendrites found at the bottom section of the FOV were due to the continuous growth of dendrites below the FOV as a consequence of the thermal gradient driven by the copper rod heat sink. The statistical analysis of the dendrite fragment volume sizes in the 2<sup>nd</sup> and the 3<sup>rd</sup> tomograms are shown in Fig. 5g and h, respectively. In particular, the total number of Al dendrite fragments with USMP in the 2<sup>nd</sup> tomogram was 1083, increased by ~100 per cent compared to that without USMP (550). These results clearly indicated that the USMP at the initial stage of solidification can lead to a significant increase in the total numbers of dendrite fragments in the melt. The morphologies of the growing dendrites, however, were quite similar for the cases with USMP and without USMP after the 3<sup>rd</sup> tomograms,

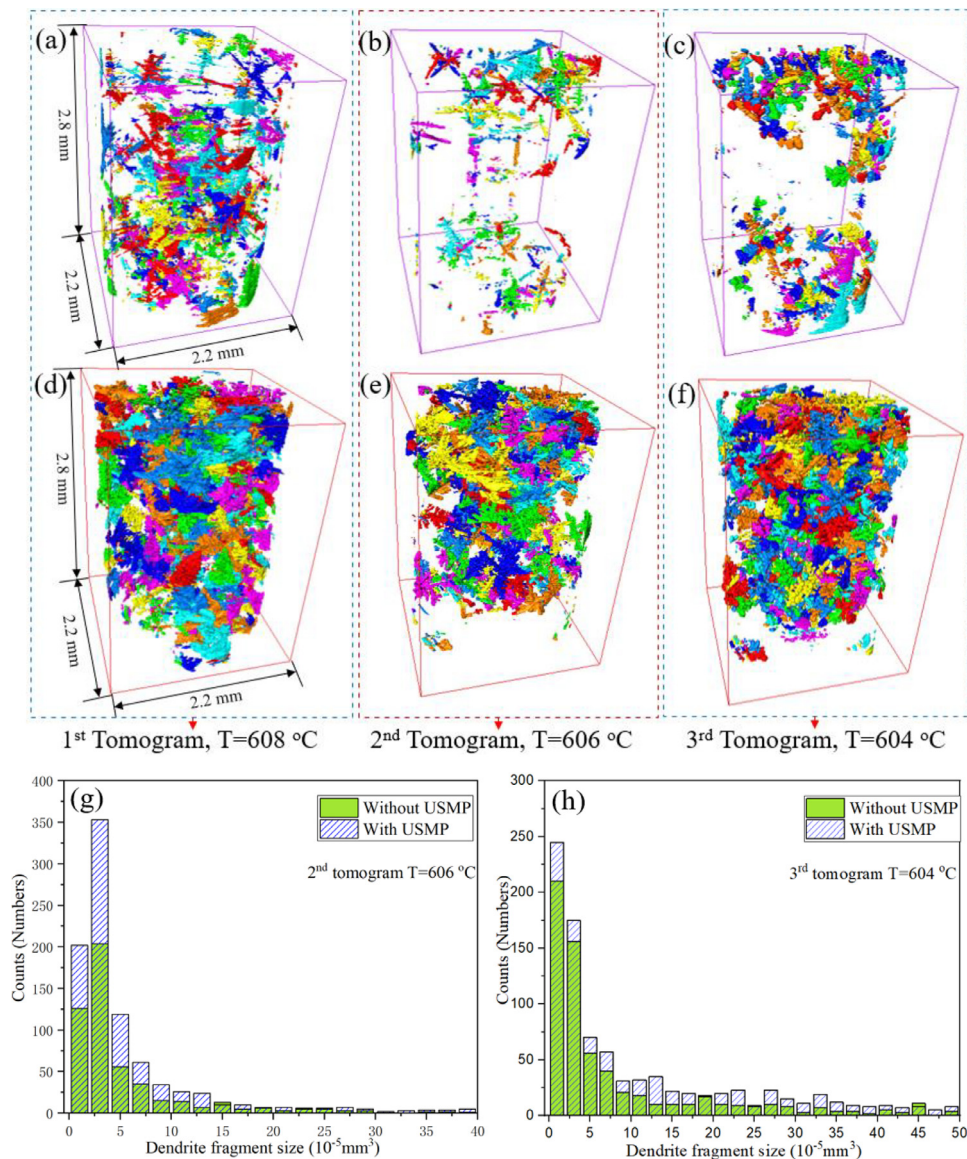


**Fig. 5.** Volume renderings of the tomography scans of the Al dendrites from the initial three tomograms immediately after the end of USMP; and the calculated dendrite volume distributions. (a), (b) and (c) are the tomography datasets without USMP; (d), (e) and (f) correspond to the tomography datasets with USMP. (g) and (h) show the dendrite fragments size distribution from the 2<sup>nd</sup> and the 3<sup>rd</sup> tomograms, respectively.

as illustrated in Fig. 5c and f. The evolution of individual dendrite is discussed in Section 3.4. Clearly, these dendrite fragments (see those visible in the view field) were seen to act as new crystal seeds to grow further as illustrated in Fig. 5c and f, resulting in refinement of the finally solidified dendritic microstructures.

### 3.3. Dendrite morphology and grain size distribution at the final stage of solidification

At the final stage of solidification, growth of the primary dendrites almost stopped and the eutectic reaction occurred. Fig. 6 and the supplementary Video #3 show the morphologies and their volume grain size distributions of the Al-15%Cu alloys at 546°C. A simple visual comparison of grain morphologies (Fig. 6a and b) indicates that the volume grain size of the Al-15%Cu alloy without USMP is larger than the case with USMP. Fig. 6c shows the volume grain size distributions. The average volume grain size for the alloy with USMP is  $3.15 \times 10^{-3} \text{ mm}^3$ , reduced by ~20 per cent compared to that without USMP ( $3.98 \times 10^{-3} \text{ mm}^3$ ).

To further quantify the grain refinement effects, 15 cross-sectional (horizontal) slices spaced evenly along the vertical direc-

tion were extracted from the final 3D tomographic datasets and the planar grain size distributions were analysed using the same algorithm as for 3D grain analysis. Such a planar grain size analysis should deliver the results that are analogous to the traditional 2D metallographic analysis. Fig. 6d shows that the average planar grain size of the alloy with USMP was  $0.9 \times 10^{-3} \text{ mm}^2$ , ~25% smaller compared to the case without USMP ( $1.2 \times 10^{-3} \text{ mm}^2$ ). Statistical analyses also indicated that, using the current separation algorithm and threshold, the 3D volume grain sizes were underestimated by approximately 3-5% when compared to the data obtained from the 2D planar grain size. The grain size distribution results in the final solidification stage clearly demonstrated that a short duration (10s) of USMP at the early stage of solidification can refine the grain size by 20-25 per cent.

### 3.4. Dendrite morphology evolution, curvature and dendrite tip growth velocity

To clarify the effects of USMP on dendrite growth dynamics, two sequences of individual dendrites at different temperatures

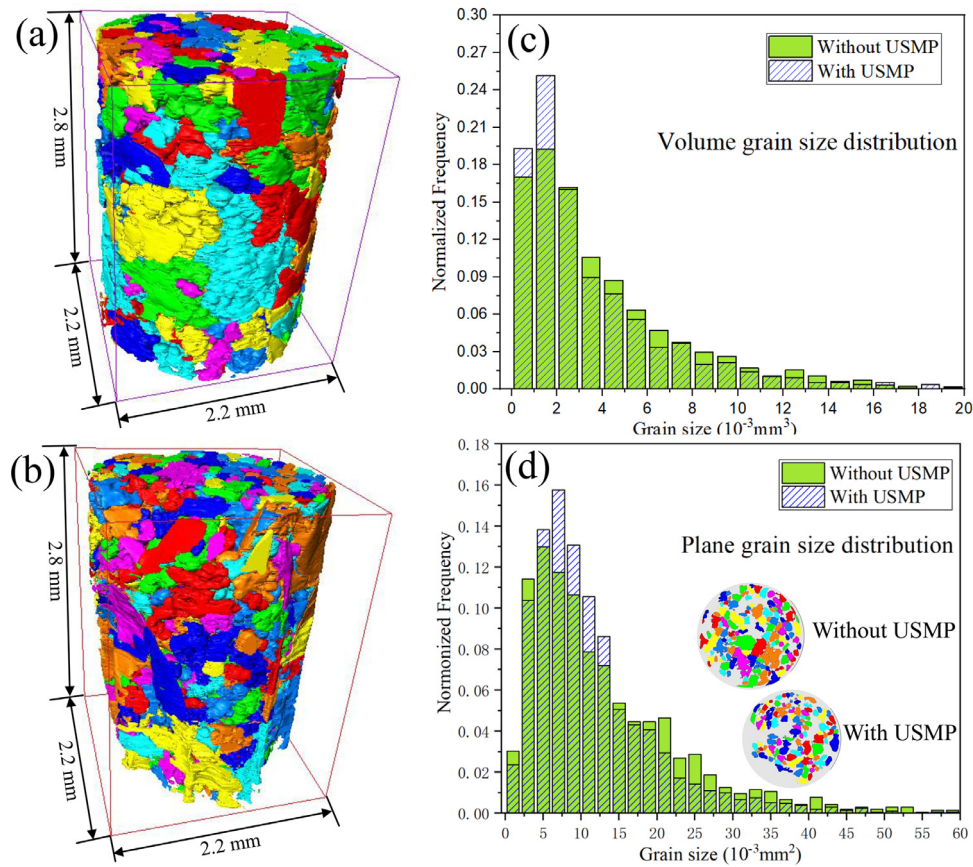


**Fig. 6.** Morphologies of the dendritic grains at the final stage of solidification for the case (a) without USMP, and (b) that with USMP. (c), the volume grain size distributions, and (d) the planar grain size distributions for both cases (see video #3 for the dendrite morphology in the whole FOV). The standard deviations for the grain size analyses were in the range of 0.5 - 0.6.

were extracted from the 3D datasets. Both dendrites were selected in the central region of the melt volume where the dendrite tip can grow into the liquid freely at the early stage of solidification. Fig. 7 and Video #4 demonstrate the time-evolved (from 606°C to 578°C) dendrite growth 3D morphologies. Note that the interface morphologies were rendered by the mean curvatures. The last dendrites were from the 16<sup>th</sup> tomogram, corresponding to the temperature at 578°C, where the dendrite free growth condition was not valid anymore because most of its dendrite arms met with other surrounding dendrite arms.

The dendrite morphology evolution for the case without USMP demonstrated that the  $\alpha$ -Al dendrites grew in four-fold crystallographic symmetry with their primary arms mutually perpendicular to each other (the central axis of the two primary arms form an orthogonal plane) in 3D space. Al dendrites are face-centred-cubic crystals which grow preferably along the low index crystal directions, e. g.,  $\langle 100 \rangle$ , since this direction has the lowest solid-liquid interfacial energy [36]. Hence, the three primary dendrite arms grew along the  $\langle 100 \rangle$  direction. Most of the secondary arms also grew along the  $\langle 100 \rangle$  direction, as shown in the figure. Small deviations from crystallographic symmetry in the secondary dendrite arms were also found, which can be attributed to the addition of Cu in the alloys since Al element possesses weak anisotropy of the solid-liquid interfacial energy that can be easily perturbed by the addition of an alloying element [37]. Fig. 7 shows that the Al dendrite maintained the four-fold symmetry structure in spite of the USMP, indicating that USMP did not alter the crystal growth orientation.

The time-evolved tomographic data also allow us to quantify the time-evolved dendrite growth kinetics. The mean curvatures

$[H = \frac{1}{2}(k_1 + k_2)]$ , where  $k_1$  and  $k_2$  are the two principal curvatures at a given point of a surface, were calculated to quantitatively characterize the solid/liquid interface evolution of the individual dendrite during solidification. The statistical results were then fitted by a Gaussian distribution function. The results of the mean curvature distribution evolution with solidification temperature (or solidification time) were illustrated in Fig. 7d and e respectively. For both cases with and without USMP, the evolutions of the mean curvature distribution profiles show a similar trend. The mean curvature distribution profiles changed from a relatively broader profile to a narrower profile with decreasing temperature. Meanwhile, the profile peak position shifted from high mean curvature to low curvature, suggesting that the interface areas with larger curvature gradually decreased with decreasing temperature. These results were in consistent with the reported solid/liquid interface evolution at the initial solidification stage [38–40]. It was due to the Gibbs-Thomson effects, which drives solute diffusion from large curve areas to small ones [41,42].

The individual dendrite volume changes as a function of temperature are presented in Fig. 7c. For the case without USMP, the rapid growth of the dendrite completed at or prior to 596°C. While for the case with USMP, growth and coarsening continued until 578°C. It is also noticed that, except for the 1<sup>st</sup> tomogram at the early stage, the individual dendrite volume in the alloy without USMP was larger than that of the USMP treated alloy when they were at the same temperatures. This can be related to the solute redistribution on the growth dynamics of the nuclei with high number density in the melt according to the free growth model [36]. As mentioned above, the initial dendrite fragment numbers in the melt without USMP were lower than those with USMP,

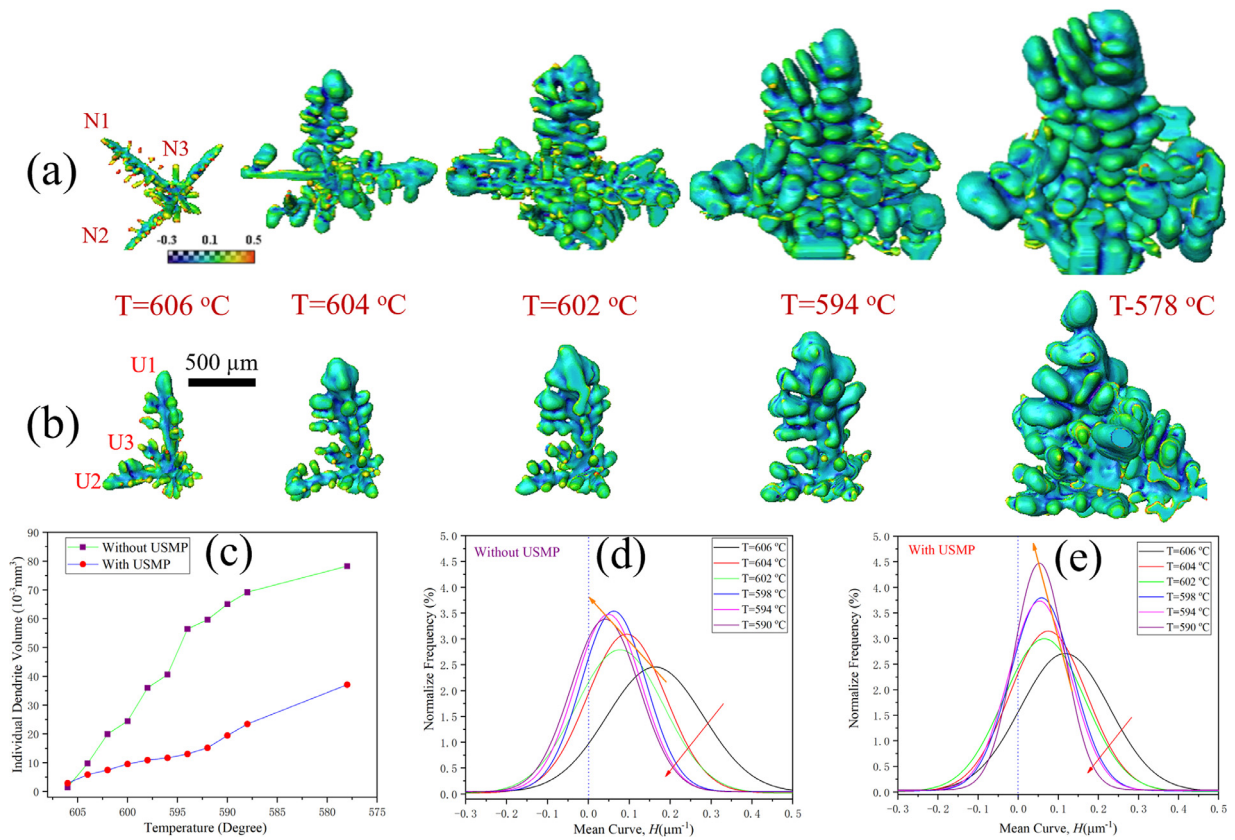


**Fig. 7.** The growth and morphology evolution of individual Al dendrites for the cases without (a) and with (b) USMP. (c) is the individual dendrite volume evolution with solidification temperature (see video #4 for the dynamic information). (d) and (e) present the mean curvature evolution with solidification temperature.

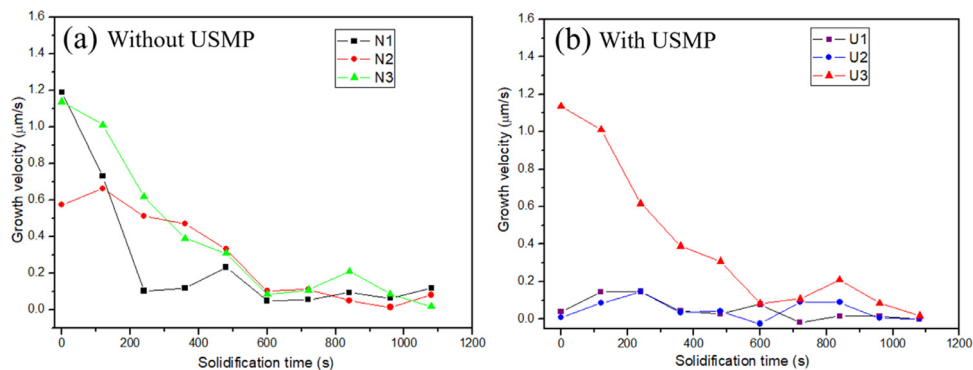


**Fig. 8.** Dendrite tip growth velocity for the three primary arms labeled in Fig. 7. (a) without USMP; (b) with USMP.

which means the Cu solute ejected from the growing Al dendrites diffused further into the melt and therefore the dendrites were able to grow faster and bigger. On the contrary, in the USMP treated melt, higher density of the fragmented dendrites means that the solute free diffusion zone around the growing dendrites was smaller and thus lowering their growth rate.

The dendrite tip growth velocity with time has been widely used to characterize dendrite growth dynamics and was useful for the validation of dendrite growth models. To calculate the dendrite tip growth velocity, the growing length of the three primary dendrite arms (labelled in Fig. 7a and b) of the two individual dendrites were measured. The dendrite tip growth velocity as a function of time is shown in Fig. 8. It is evident that the dendrite tip growth velocity varied for different arms, which was related to the different conditions between the adjacent dendrites during growth. By observing the neighbourhood environment of the selected den-

drite arms over time in 3D datasets, it was found that larger free space in the melt led to a higher growth velocity. The growth velocity of U3 primary arm in the USMP treated melt was quite similar to those of N1 and N3 primary arms in the melt without USMP, suggesting the liquid constituent in that growing direction was similar to those without USMP. The gradually slowing down of the dendrite tip growth velocity was attributed to the constraints imposed by the solute distribution in front of the solid-liquid interface, which mainly depended on the interactions with other dendrites [43]. Similar growth rate phenomena over time were reported in Al-Si [44] and Mg-Sn alloys [41].

Fig. 9 shows the vicinity of the selected Al primary dendrites at the 6<sup>th</sup> tomogram (598°C), indicating some of the primary arms grew closer to the nearest neighbour dendrites. Also the nearest neighbour dendrites in the alloy with USMP (Fig. 9b, d) were more than the alloy without USMP (Fig. 9a, c), which might constrain

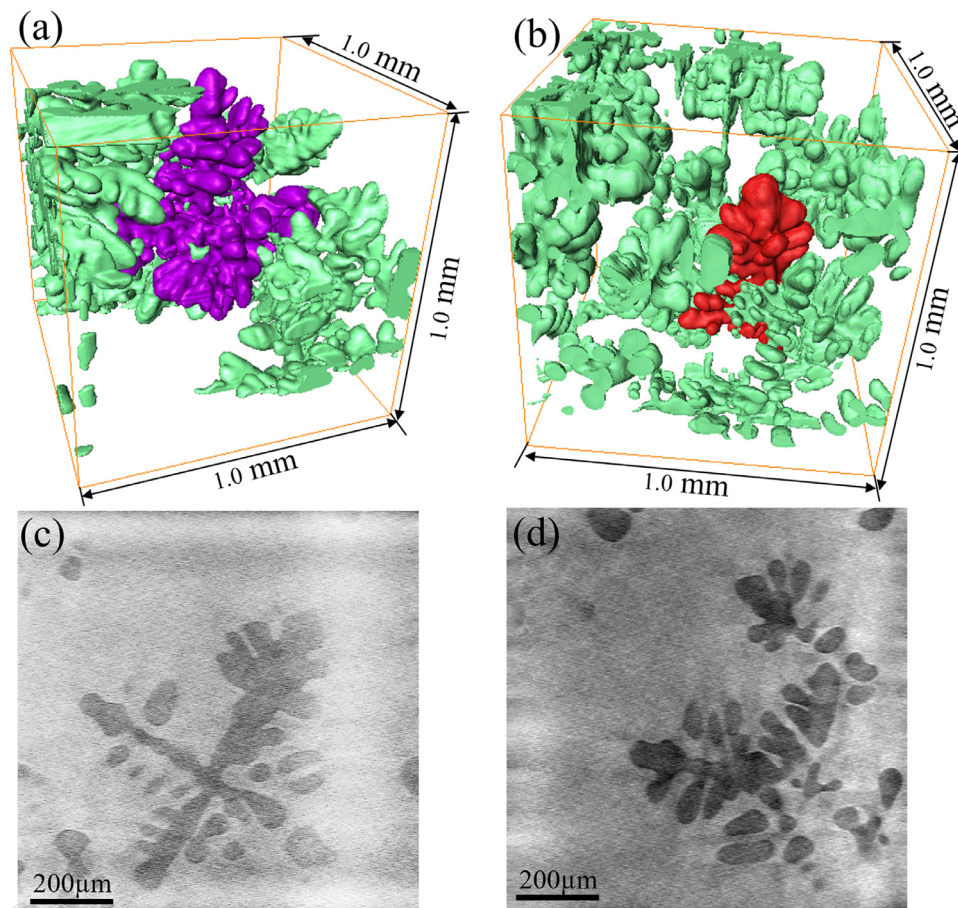


**Fig. 9.** The vicinity of the selected Al primary dendrites from the 6<sup>th</sup> tomogram at 598 °C; (a), (c) without USMP; (b), (d) with USMP.

their further growth in the preferred growth directions. The 2D slices containing the selected dendrites extracted from the 3D tomograms show the similar characteristic as well (comparing Fig. 9c with Fig. 9d). More dendrites in the USMP case resulted in higher Cu content (darker region in Fig. 9d) in front of the dendrite interface, leading to a lower growth velocity.

## 4. Discussion

### 4.1. The mechanism of dendrite fragmentation under USMP

A number of studies including experiments and simulations have been conducted to investigate the dendrite fragmentation mechanisms in the presence of ultrasound fields [6,9,12,17,45,46]. The results observed using ultrafast synchrotron X-ray imaging [9] and high-speed optical imaging [24] revealed that the shock wave pressure produced at bubble implosion can break up solid phases instantly. The cyclic force due to individual oscillating bubble or bubble clouds can initiate cracks first in the solid phases, and then fracture them by the fatigue effect in a few thousands of ultrasound cycles (normally in hundreds of milliseconds). The acoustic flow was also found to be effective in breaking up the liquid-solid interface in some specific conditions as described in Ref. [9]. However, most previous studies found that acoustic flow mainly played a role in transferring or recirculating the fragmented phases throughout the melt volume. In the present study, using a specially designed sample holder and under the applied ultrasound intensity, significantly enhanced acoustic swirling flow was clearly observed within the FOV. Efficient dendrite fragmentation events were also observed to occur continuously under the action of the

swirling flow in the 10 s period of USMP (those frames in Video #1 after 330 ms). In contrast, in the condition without USMP, no visible dendrite fragmentation events in the FOV were observed (the frames in Video #1 prior to 330 ms). Hence, the real-time and *in situ* observation illustrated unambiguously that the dendrite fragmentation in this case was caused by the strong acoustic flow. Further examination of the morphology evolution of the long dendrite arm (Fig. 4 and Video #2) illustrated that (1) the long primary dendrite arm moved to the left side of the FOV (from Fig. 3a to b) under the impact of the acoustic flow; (2) its area fraction was reduced by 42.5% in 10 s (occurred gradually from the arm tip downwards) under the continuous action of the swirling flow. Video #2 also showed that, apart from the expected thermal perturbation in the melt due to the applied ultrasound (typically a few degrees as illustrated in Fig. 2 of Ref. [9]), the only dominant visible phenomenon was the swirling flow's impact onto the long dendrite arm.

To estimate approximately the magnitude of the force acting onto the long dendrite arm caused by the swirling flow, a simple model proposed by Pilling and Hellawell [47] was used. In this model, a cylindrical dendrite with length  $L$  and radius  $r$  is fixed at one end, while the other end is free (the schematic of this model was presented in our previous study [17]). Such simple geometric model captures the main characteristics of the long dendrite arm shown in Fig. 3b. A flow with a velocity  $v$  passing across the radial direction will result in a stress  $\sigma$  on the section of the cylindrical dendrite. The maximum bending stress can be calculated by [17,47]:

$$\sigma = \frac{6\eta v L^2}{r^3}$$

Where  $\eta$  is the dynamic viscosity. According to Ref. [48], the viscosity of Al-15%Cu alloy at  $-610^{\circ}\text{C}$  is estimated as  $\sim 1.51 \times 10^{-3}$  Pa s. The velocity of the acoustic flow is  $\sim 0.3$  m/s. The typical  $L$  and  $r$  values are taken as 1000 and  $20 \mu\text{m}$ , respectively, as measured from the dendrite fragments in 2D radiography images. Based on the above parameter values, the maximum bending stress at the dendrite root was calculated as  $\sim 2.72$  MPa; while away from the root area, for instance, in the midway towards the dendrite tip, the bending stress was calculated as  $\sim 0.68$  MPa.

For the Al-15%Cu alloy, the Al-rich solid dendrites appeared in the FOV at  $-610^{\circ}\text{C}$ . At this temperature, the Cu composition in the Al-rich dendrite is about  $\sim 2.5\%$  (calculated from the Al-Cu binary phase diagram [29]). The fracture strength of the single crystal Al-2.5Cu dendrites at the temperature close to its melting point was evaluated to be less than 1 MPa from the in-situ X-ray radiography (see Section 3 of the Supplementary Materials).

Therefore, from a simple mechanical point of view, many secondary and tertiary dendrite arms (especially at their roots areas) at the temperature close to the melting point do not have sufficient strength to withstand any tensile or shear stresses higher than a few MPa. The reasons are explained below.

Dendrites are not uniform structure but have hierarchical dendritic arms at the microscopic level. The rejected Cu solute due to the growth of Al-rich dendrites is often trapped in the gaps between the adjacent dendrite arms, especially at the root regions of the dendrite arms where the diffusion of Cu solutes is limited. These Cu-rich regions have lower local melting temperature compared to that of the dendrite trunk. Therefore, a very small temperature perturbation (induced by fluid agitation or external forces) could accelerate dendrite remelting or high-order dendrite arm detachment at the dendrite roots (or tips). This is a well-understood thermal-solute remelting phenomenon. Real-time observations of such dendrite remelting and fragmentation phenomena were reported in Ref [26,50]. In those experiments, dendrite fragmentation of Al-15Cu alloys was observed to occur in a time scale from tens of to hundreds of seconds [26,49] under a quasi-static solidification condition. Such slow fragmentation events (typically shown in Fig. 5 and Fig. 7 in Ref. [49]) and the slightly detaching of the secondary or tertiary dendrite arms from their primary dendrite trunk did not turn them into effective new crystal seeds in the subsequent solidification process. Because those fragmented or remelted dendrites could re-join the main trunk when the melt was further cooled down.

The ultrasound induced swirling flow observed in this study played a crucial role in not only creating abundant new dendrite fragments, but also concurrently turning them into the effective new crystal seeds through the combined thermal remelting plus mechanical fracture and separation mechanism. The real time evidence with a millisecond resolution supports the following mechanism: first, the enhanced acoustic flow ( $\sim 0.3$  m/s) was quickly enough to sweep through the growing dendrites in less than a millisecond, causing temperature perturbation (in a time scale of tens of millisecond). Therefore, remelting events on the dendrite roots occurred in tens of millisecond. After that, the force generated by the acoustic flow effectively broke up the dendrites at the remelting points and carried them away to other regions of the melt, making the dendrite fragments to become new crystal seeds. Video #1 clearly demonstrated that free and floating dendrite fragments appeared in the FOV within tens of milliseconds after the application of ultrasound (it is recommended to use Fiji software to import the video so that every frame can be viewed and tracked). Hence, the dendrite fragmentation and separation events shown in this study were the combined thermal remelting plus mechanical fracture and separation effects occurred in tens of millisecond time scale. This mechanism is unique to ultrasound melt processing compared to other dendrite fragmentation phenomena where

only gravity or magnetic field forced convection was present in the solidification process [49]. The dendrite fragmentation events in these cases occurred in a time scale at least 100 or even 1000 times slower than those occurred in the ultrasound melt processing.

In addition to the combined thermal remelting plus mechanical fracture effects, The swirling flow driven by the alternating acoustic pressure field behaved in a cyclic manner, exerting cyclic fatigue impact force onto the growing dendrites. This effect was seen clearly by the cyclic swaying movement of the cellular grain cluster in Fig. 3a, b and c. The grain cluster was broken up gradually in less than 1 s (Video #1), releasing many tiny fragments into the circulating melt. Also evidenced in Video #1 were the frequent collision events among the fast-moving solid dendrite fragments in the acoustic flow field, which were also effective in producing more dendrite fragments. However, statistical analysis showed that, dendrite fragmentation events due to the swirling flow fatigue effect or solid phases collision were much less compared to those caused by the more universal thermal perturbation plus mechanical fracture effects.

In summary, under the current experimental conditions, acoustic flow induced thermal perturbation remelting plus mechanical fracture is the dominant mechanism for dendrite fragmentation in USMP. Other mechanisms such as solid phase collision and cyclic flow fatigue effects are the less dominant mechanisms.

#### 4.2. Effects of USMP on redistribution of the dendrite fragments in the melt

In cases where there is no other external force involved, the growth of the primary dendrites would be restricted to the vicinity of their original nucleation sites. In the present study, the solidification of Al-15%Cu alloy without USMP demonstrated such a case, resulting in coarse grains in the solidified samples. Therefore, external fields such as electromagnetic and ultrasonic fields were often introduced to alter the distribution of the primary phases or dendrites [5,7,49–51]. The application of ultrasound in this case was seen to change effectively the distribution of the primary Al dendrite fragments in the FOV by the swirling acoustic flow (Video #1 and Fig. 5). For achieving a uniform distribution of the fragmented dendrites, the swirling flow was much beneficial in countering the gravity effect, because radiography and tomography clearly showed that, once the USMP stopped, the primary Al dendrite fragments tended to float up to the top of the FOV due to the density difference between the primary Al dendrite fragments and that of the melt.

#### 4.3. Effects of USMP on the dendrite growth

The entire tomography sequence from the termination of USMP to the end of solidification provided a set of consistent and rich 3D datasets. A systematic analysis indicated that the microstructure refinement mainly resulted from the increased number of dendrite fragments caused by the USMP at the early stage of solidification, which was almost twice of the fragment numbers in the case without USMP. In the studied condition, these dendrite fragments were mainly induced by the acoustic streaming flow in 10 s.

In addition, remelting and fragmentation of the growing primary dendrites as well as the strong stirring effect of the acoustic swirling flow affected the composition distribution of the Cu in the remaining liquid melt. Fig. 9d shows that higher number of dendrite fragments in the USMP case resulted in higher Cu content in front of the dendrites and less liquid volume among the dendrites for further free growth. Such combined effects would lead to a lower growth rate in some of the growing directions (i.e. U1 and U2 in Fig. 8b) for the dendrites fragments. Although the growth

orientation of the Al dendrites did not change because of USMP. Certainly, the slowed dendrite growth rate would also contribute, although in a much less extent, to the finally grain refinement.

## 5. Conclusions

The dendrite fragmentation dynamics of an Al-15%Cu alloy during solidification under ultrasound was studied *in situ* and real time by high-speed synchrotron X-ray imaging. The 4D (3D space plus time) dendrite fragments distribution, morphology and growth rate were investigated and quantified using ultrafast synchrotron X-ray tomography. The combined techniques were able to visualize continuously the whole solidification process of the Al-15%Cu alloy in a meaningful melt volume. The research generated very rich real-time 3D and 4D datasets that are valuable for further validation of numerical models and assistance of industrial application of USMP. The important and new quantitative findings of this research are:

1. The applied ultrasound produced an enhanced acoustic swirling flow with an average velocity of 0.3 m/s. It was the dominant driving force for producing dendrite fragmentation due to the thermal perturbation induced remelting plus mechanical fracture and separation. This is the dominant mechanism for producing dendrite fragments at the early stage of solidification under ultrasound.
2. Driven by the alternating acoustic pressure field, the swirling flow behaved in a cyclic manner, exerting cyclic fatigue force on the growing dendrites in the melt. Solid phase collisions also frequently occurred inside the swirling flow. The fatigue and collisions effects are the less dominant but important mechanisms in producing dendrite fragmentation.
3. The instantaneous 3D morphology and distribution of dendrite fragments immediately after USMP were quantified and reported. Compared to the case without USMP, 10 s of USMP resulted in an increase of ~100% dendrite fragments in the melt at the early stage of solidification. Such grain multiplication effects resulted in 20–25% reduction in the average grain size in the solidified alloy samples.
4. In the studied conditions, the application of ultrasound did not show any obvious effect on altering the preferred crystallographic growth direction of the Al dendrites. But it homogenized dendrite fragments distribution and thus decreased dendrite growth rate, which is also beneficial for the grain refinement.

## Declaration of Competing Interest

We declare that there is no conflict of interest among all authors concerning the submitted manuscript.

## Acknowledgments

The authors wish to make the following acknowledgements: **Project Funding & Financial Support:** UK Engineering and Physical Sciences Research Council (Grant No. EP/L019965/1), the Royal Society Industry Fellowship (for J. Mi in 2012–2016), and the Chinese Scholarship Council (Funding No. 201806785038 for Z. Zhang's visiting fellowship at the University of Hull in the academic year 2019–2020). Facility Access: Paul Scherrer Institut, Villigen, Switzerland for provision of synchrotron radiation beamtime (proposal number 20141167, 20150177, 20160284) at the TOMCAT beamline X02DA of the Swiss Light Source. **Technical Support:** Staff at University of Hull and Diamond Light Source who helped to prepare the equipment and run the experiments, specifically Bob Greening of Diamond for machining some of the specially designed

niobium sonotrodes, Thomas Connolley and Phoebe Allan of Diamond for assistance in running the experiment at TOMCAT. Access to the Viper High Performance Computing facility of the University of Hull and the support from its technical team as well as Dr. Nghia T. Vo who carried out some reconstruction work of the X-ray tomography datasets.

## Supplementary materials

Supplementary material associated with this article can be found, in the online version, at doi:10.1016/j.actamat.2021.116796.

## References

- [1] G.I. Eskin, Broad prospects for commercial application of the ultrasonic (cavitation) melt treatment of light alloys, *Ultrason. Sonochem.* 8 (2001) 319–325.
- [2] G.I. Eskin, D.G. Eskin, *Ultrasonic Treatment of Light Alloy Melts*, second ed., CRC Press, Florida, 2015.
- [3] D.G. Eskin, J. Mi, *Solidification Processing of Metallic Alloys Under External Fields*, Springer Nature Switzerland AG, London, 2018.
- [4] D.G. Eskin, I. Tzanakis, F. Wang, G.S.B. Lebon, T. Subroto, K. Pericleous, J. Mi, Fundamental studies of ultrasonic melt processing, *Ultrason. Sonochem.* 52 (2019) 455–467.
- [5] W. Mirihanage, Wenwu, J. Tamayo, D. Eskin, M. Garcia-Fernandez, P. Srirangam, P. Lee, Synchrotron radiographic studies of ultrasonic melt processing of metal matrix nanocomposites, *Mater. Lett.* 164 (2016) 484–487.
- [6] T.V. Atamanenko, D.G. Eskin, L. Zhang, L. Katgerman, Criteria of grain refinement induced by ultrasonic melt treatment of aluminium alloys containing Zr and Ti, *Metall. Mater. Trans. A* 41 (2010) 2056–2066.
- [7] L. Zhang, D.G. Eskin, L. Katgerman, Influence of ultrasonic melt treatment on the formation of primary intermetallics and related grain refinement in aluminium alloys, *J. Mater. Sci.* 46 (2011) 5252–5259.
- [8] D. Wang, M.P. De Cicco, X. Li, Using diluted master nanocomposites to achieve grain refinement and mechanical property enhancement in as-cast Al-9Mg, *Mater. Sci. Eng. A* 532 (2012) 396–400.
- [9] B. Wang, D. Tan, T.L. Lee, J. Khong, F. Wang, D. Eskin, T. Connolley, K. Fezzaa, J. Mi, Ultrafast synchrotron X-ray imaging studies of microstructure fragmentation in solidification under ultrasound, *Acta Mater* 144 (2018) 505–515.
- [10] C.J. Todaro, M.A. Easton, D. Qiu, D. Zhang, M.J. Bermingham, E.W. Lui, M. Brandt, D.H. StJohn, M. Qian, Grain structure control during metal 3D printing by high-intensity ultrasound, *Nat. Commun.* 11 (2020) 142.
- [11] T.L. Lee, J.C. Khong, K. Fezzaa, J. Mi, Ultrafast X-ray imaging and modelling of ultrasonic cavitations in liquid metal, *Mater. Sci. Forum* 765 (2013) 190–194.
- [12] D. Tan, T.L. Lee, J.C. Khong, T. Connolley, K. Fezzaa, J. Mi, High-speed synchrotron x-ray imaging studies of the ultrasound shockwave and enhanced flow during metal solidification processes, *Metall. Mater. Trans. A* 46 (2015) 2851–2861.
- [13] J. Mi, D. Tan, T.L. Lee, In situ synchrotron x-ray study of ultrasound cavitation and its effect on solidification microstructures, *Metall. Mater. Trans. B* 46 (2015) 1615–1619.
- [14] H. Huang, D. Shu, Y. Fu, J. Wang, B. Sun, Synchrotron radiation X-ray imaging of cavitation bubbles in Al-Cu alloy melt, *Ultrason. Sonochem.* 21 (2014) 1275–1278.
- [15] W.W. Xu, I. Tzanakis, P. Srirangam, W.U. Mirihanage, D.G. Eskin, A.J. Bodey, P.D. Lee, Synchrotron quantification of ultrasound cavitation and bubble dynamics in Al-10Cu melts, *Ultrason. Sonochem.* 31 (2016) 355–361.
- [16] I. Tzanakis, W.W. Xu, D.G. Eskin, P.D. Lee, N. Kotsovinos, In situ observation and analysis of ultrasonic capillary effect in molten aluminium, *Ultrason. Sonochem.* 27 (2015) 72–80.
- [17] F. Wang, D. Eskin, J. Mi, C. Wang, B. Koe, A. King, C. Reinhard, T. Connolley, A synchrotron X-radiography study of the fragmentation and refinement of primary intermetallic particles in an Al-35Cu alloy induced by ultrasonic melt processing, *Acta Mater* 141 (2017) 142–153.
- [18] D. Tolnai, P. Townsend, G. Requena, L. Salvo, J. Lendvai, H.P. Degischer, In situ synchrotron tomographic investigation of the solidification of an AlMg<sub>4</sub>Si<sub>8</sub> alloy, *Acta Mater* 60 (2012) 2568–2577.
- [19] O. Ludwig, M. Dimichiel, L. Salvo, M. Suery, P. Falus, In-situ three-dimensional microstructural investigation of solidification of an Al-Cu alloy by ultrafast X-ray microtomography, *Metall. Mater. Trans. A* 36 (2005) 1515–1523.
- [20] C. Puncreobutr, A.B. Phillion, J.L. Fife, P. Rockett, A.P. Horsfield, P.D. Lee, In situ quantification of the nucleation and growth of Fe-rich intermetallics during Al alloy solidification, *Acta Mater* 79 (2014) 292–303.
- [21] S.S. Shuai, E.Y. Guo, M.Y. Wang, M.D. Callaghan, T. Jing, Q.W. Zheng, P.D. Lee, Anomalous alpha-Mg dendrite growth during directional solidification of a Mg-Zn alloy, *Metall. Mater. Trans. A* 47A (9) (2016) 4368–4373.
- [22] M.H. Yang, S.M. Xiong, Z.P. Guo, Effect of different solute additions on dendrite morphology and orientation selection in cast binary magnesium alloys, *Acta Mater* 112 (2016) 261–272.
- [23] S.S. Shuai, E.Y. Guo, Q.W. Zheng, M.Y. Wang, T. Jing, Y.N. Fu, Three-dimensional a-Mg dendritic morphology and branching structure transition in Mg-Zn alloys, *Mater. Charact.* 118 (2016) 304–308.

- [24] D. Shu, B. Sun, J. Mi, P.S. Grant, A high-speed imaging and modelling study of dendrite fragmentation caused by ultrasonic cavitation, *Metall. Mater. Trans. A* 43A (2012) 3755–3766.
- [25] S. Wang, J. Kang, Z. Guo, T.L. Lee, X. Zhang, Q. Wang, C. Deng, J. Mi, In situ high speed imaging study and modelling of the fatigue fragmentation of dendritic structures in ultrasonic fields, *Acta Mater.* 165 (2019) 388–397.
- [26] B. Cai, J. Wang, A. Kao, K. Pericleous, A.B. Phillion, R.C. Atwood, P.D. Lee, 4D synchrotron X-ray tomographic quantification of the transition from cellular to dendrite growth during directional solidification, *Acta Mater.* 117 (2016) 160–169.
- [27] M. Stampanoni, A. Groso, A. Isenegger, G. Mikuljan, Q. Chen, A. Bertrand, S. Henein, R. Betemps, U. Frommherz, P. Bohler, D. Meister, M. Lange, R. Abela, Trends in synchrotron-based tomographic imaging: the SLS experience, developments in X-ray tomography V, *Proceed. Soc. Photo-Opt. Instrum. Eng. (SPIE)* 6318 (2006) U199–U212.
- [28] R. Mokso, C.M. Schlepütz, G. Theidel, H. Billich, E. Schmid, T. Celcer, et al., GigaFRoST: the gigabit fast readout system for tomography, *J. Synchrotron Rad.* 24 (6) (2017) 1250–1259.
- [29] O. Zobac, A. Kroupa, A. Zemanova, K.W. Richter, Experimental description of the Al-Cu binary phase diagram, *Metall. Mater. Trans. A* 50A (2019) 3805–3815.
- [30] J. Schindelin, I. Arganda-Carreras, E. Frise, et al., Fiji: an open-source platform for biological-image analysis, *Nat. Methods* 9 (7) (2012) 676–682.
- [31] S.R. Stock, *Micro Computed Tomography: Methodology and Applications*, CRC Press, 2008.
- [32] C. Atwood Robert, J. Bodey Andrew, W.T. Price Stephen, B. Mark, D. Michael, A high-throughput system for high-quality tomographic reconstruction of large datasets at diamond light source, *Phil. Trans. R. Soc. A* 373 (2015) 20140398.
- [33] W. van Aarle, W.J. Palenstijn, J. Cant, E. Janssens, F. Bleichrodt, A. Dabrovolski, J. De Beenhouwer, K. Joost Batenburg, J. Sijbers, Fast and flexible X-ray tomography using the ASTRA toolbox, *Opt. Express* 24 (22) (2016) 25129–25147.
- [34] Zuiderveld, K., *Contrast limited Adaptive Histogram Equalization*, *Graphics Gems IV*, Academic Press Professional, Inc., Cambridge, 994, pp. 474–485.
- [35] E. Riedel, M. Liepe, S. Scharf, Simulation of ultrasonic induced cavitation and acoustic streaming in liquid and solidifying aluminum, *Metals* 10 (2020) 476–499.
- [36] J. Friedli, J. Fife, P. Di Napoli, M. Rappaz, Dendritic growth morphologies in Al-Zn alloys-part I: X-ray tomographic microscopy, *Metall. Mater. Trans. A* 44 (2013) 5522–5531.
- [37] S. Liu, R.E. Napolitano, R. Trivedi, Measurement of anisotropy of crystal-melt interfacial energy for a binary Al-Cu alloy, *Acta. Mater.* 49 (2001) 4271–4276.
- [38] J.L. Fife, J.W. Gibbs, E.B. Gulsoy, C.L. Park, K. Thornton, P.W. Voorhees, The dynamics of interfaces during coarsening in solid-liquid systems, *Acta Mater* 70 (2014) 66–78.
- [39] D. Kammer, P.W. Voorhees, The morphological evolution of dendritic microstructures during coarsening, *Acta Mater.* 54 (2006) 1549–1558.
- [40] S. Terzi, L. Salvo, M. Suery, A.K. Dahle, E. Boller, Coarsening mechanisms in a dendritic Al-10% Cu alloy, *Acta Mater.* 58 (2010) 20–30.
- [41] S. Shuai, E. Guo, A.B. Phillion, M.D. Callaghan, T. Jing, P.D. Lee, Fast synchrotron X-ray tomographic quantification of dendrite evolution during the solidification of Mg-Sn alloys, *Acta Mater.* 118 (2016) 260–269.
- [42] R. Mendoza, I. Savin, K. Thornton, P.W. Voorhees, Topological complexity and the dynamics of coarsening, *Nat. Mater.* 3 (2004) 385–388.
- [43] Da Shu, Baode Sun, J. Mi, P.S. Grant, A quantitative study of solute diffusion field effects on heterogeneous nucleation and the grain size of alloys, *Acta Mater.* 59 (2011) 2135–2144.
- [44] A. Prasad, S.D. McDonald, H. Yasuda, K. Nogita, D.H. StJohn, A real-time synchrotron X-ray study of primary phase nucleation and formation in hypoeutectic Al-Si alloys, *J. Cryst. Growth* 430 (2015) 122–137.
- [45] G. Wang, Q. Wang, N. Balasubramani, M. Qian, D.G. Eskin, M.S. Dargusch, D.H. StJohn, The role of ultrasonically induced acoustic streaming in developing fine equiaxed grains during the solidification of an Al-2 Pct Cu alloy, *Metall. Mater. Trans. A* 50 (2019) 5253–5263.
- [46] H.R. Kotadia, M. Qian, D.G. Eskin, A. Das, On the microstructural refinement in commercial purity Al and Al-10wt% Cu alloy under ultrasonication during solidification, *Mater. Des.* 132 (2017) 266–274.
- [47] J. Pilling, A. Hellawell, Mechanical deformation of dendrites by fluid flow, *Metall. Mater. Trans. A* 27 (1996) 229–232.
- [48] S. Ganesan, R. Speiser, D.R. Poirier, Viscosities of aluminum-rich Al-Cu liquid alloys, *Metall. Trans. B* 18 (1987) 421–424.
- [49] E. Liotti, A. Lui, R. Vincent, S. Kumar, Z. Guo, T. Connolley, I.P. Dolbnya, M. Hart, L. Arnberg, R.H. Mathiesen, P.S. Grant, A synchrotron X-ray radiography study of dendrite fragmentation induced by a pulsed electromagnetic field in an Al-15Cu alloy, *Acta Mater.* 70 (2014) 228–239.
- [50] E. Guo, S. Shuai, D. Kazantsev, S. Karagadde, A.B. Phillion, T. Jing, W. Li, P.D. Lee, The influence of nanoparticles on dendritic grain growth in Mg alloys, *Acta Mater.* 152 (2018) 127–137.
- [51] T. Campanella, C. Charbon, M. Rappaz, Grain refinement induced by electromagnetic stirring: a dendrite fragmentation criterion, *Metall. Mater. Trans. A* 35 (2004) 3201–3210.